ADVANCES IN ATMOSPHERIC SCIENCES, VOL. 34, APRIL 2017, 559–570

• **Original Paper** •

Analysis of a Vortex Precipitation Event over Southwest China Using AIRS and In Situ Measurements

Chengcheng NI[1,2], Guoping LI[*1,3], and Xiaozhen XIONG[4]

[1]*School of Atmospheric Sciences, Chengdu University of Information Technology, Chengdu* 610225*, China*
[2]*Meteorological Observatory, Chengdu Meteorological Bureau, Chengdu* 610072*, China*
[3]*Collaborative Innovation Center on Forecast and Evaluation of Meteorological Disasters, Nanjing University of Information Science and Technology, Nanjing* 210044*, China*
[4]*Centre of Satellite Application and Research, NOAA, College Park, MD* 20740*, USA*

(Received 21 June 2016; revised 5 October 2016; accepted 4 November 2016)

ABSTRACT

A strong precipitation event caused by the southwest vortex (SWV), which affected Sichuan Province and Chongqing municipality in Southwest China on 10–14 July 2012, is investigated. The SWV is examined using satellite observations from AIRS (Atmospheric Infrared Sounder), in situ measurements from the SWV intensive observation campaign, and MICAPS (Marine Interactive Computer-Aided Provisioning System) data. Analysis of this precipitation process revealed that: (1) heavy rain occurred during the development phase, and cloud water content increased significantly after the dissipation of the SWV; (2) the area with low outgoing longwave radiation values from AIRS correlated well with the SWV; (3) variation of the temperature of brightness blackbody (TBB) from AIRS reflected the evolution of the SWV, and the values of TBB reduced significantly during the SWV's development; and (4) strong temperature and water vapor inversions were noted during the development of the SWV. The moisture profile displayed large vertical variation during the SWV's puissant phase, with the moisture inversion occurring at low levels. The moisture content during the receding phase was significantly reduced compared with that during the developing and puissant phases. The vertical flux of vapor divergence explained the variation of the moisture profile. These results also indicate the potential for using AIRS products in studying severe weather over the Tibetan Plateau and its surroundings, where in situ measurements are sparse.

Key words: precipitation event, AIRS, southwest vortex, temperature profile, moisture profile

Citation: Ni, C. C., G. P. Li, X. Z. Xiong, 2017: Analysis of a vortex precipitation event over Southwest China using AIRS and in situ measurements. *Adv. Atmos. Sci.*, **34**(4), 559–570, doi: 10.1007/s00376-016-5262-4.

1. Introduction

The distribution and movement of rain bands and torrential rain in China are closely related to seasonal abrupt changes in the atmosphere over eastern Asia (Chang et al., 2000). Torrential rain in this region is largely attributable to the thermal and dynamic forcing of the Tibetan Plateau (TP) (Gao and Ping, 2005). These synoptic systems result in extreme weather events over the TP and significantly affect the related precipitation that falls in other regions of China and Asia (Tao and Ding, 1981; Kuo et al., 1986). Meso-α-scale vortices (Orlanski, 1975) that form near the TP are among the most important rain-producing systems in China during the warm season. Only a small proportion of these systems are able to migrate eastward from southwestern China and develop into severe weather systems that cause flooding along their paths (Kuo et al., 1988). The Southwest Vortex (SWV), which is a mesoscale vortex over Southwest China, forms primarily at 700 hPa at the eastern flanks of the TP and the Sichuan Basin (Wang and Orlanski, 1987; Li et al., 2014; Fu et al., 2015). Torrential rain in Southwest China is usually associated with the formation and development of the SWV. This system originates from the combined influence of the TP's topography and the mid-scale terrain of the Western Sichuan Plateau (Wang and Tan, 2014). The influence of the SWV on torrential rain has been widely studied in terms of understanding its generation, movement, circulation structure, and mesoscale characteristics (Chang et al., 2000; Li, 2007; He, 2012; Zhong et al., 2014)., with some studies having been based on CFSR (Climate Forecast System Reanalysis) data for a long period. Additionally, the climatic characteristics of SWVs and DBVs (Dabie vortices) have been analyzed (Zhang et al., 2015), and four types of SWV have been classified according to their dynamic and thermodynamic features (Fu et al., 2015). Additionally, some

* Corresponding author: Guoping LI
Email: liguoping@cuit.edu.cn

studies having been based on CFSR (Climate Forecast System Reanalysis) data for a long period (Fu et al., 2015; Zhang et al., 2015). The climatic characteristics of SWVs and DBVs (Dabie vortices) have been analyzed, and four types of SWV have been classified according to their dynamic and thermodynamic features.

The mei-yu (baiyu) front is a predominantly convective baroclinic zone that spans for thousands of kilometers from East China into the western Pacific Ocean south of Japan. Previous research has demonstrated a relationship between the SWV and this front under the situation of the onset of the summer Indian monsoon (Chen and Gao, 2007). Several researchers have investigated the evolution the SWV in the lee of the TP under certain atmospheric circulation (Kuo et al., 1986; Wang et al., 1993) and have revealed that the western Pacific subtropical high expands westward at 500 hPa and that the trough in the lee of the TP is amplified by potential vorticity. The results of these studies have indicated that adiabatic heating driven by mesoscale convection induces SWV development. By using a limited-area mesoscale numerical model, researchers have revealed the common features between the dynamic structures in model simulations and observations, and that the terrain effect plays a crucial role in SWV development in the Sichuan Basin (Wang and Orlanski, 1987; Chang et al., 2000).

In recent years, regional rainstorms caused by the SWV have increased the occurrence frequency of secondary geological disasters such as floods, debris flows and landslides, and have become primary disastrous weather events in Southwest China during summer. Thus, it is imperative to conduct additional studies on the SWV. However, owing to the limitations of surface measurements and sounding data over the TP, an increasing number of studies have employed satellite data for studying SWV dynamics and transport.

The Atmospheric Infrared Sounder (AIRS) was launched into sun synchronous polar orbit 2130 UTC, ascending node) by NASA on the EOS/Aqua satellite on 4 May 2002. This instrument provides atmospheric temperature measurements and water vapor profiles with high accuracy, as well as surface temperature and cloud information. Designed to measure Earth's atmospheric water vapor and temperature profiles on a global scale, AIRS has 2378 channels and nominally acquires measurements over the entire globe twice daily. Many researchers have compared AIRS water vapor data with other measurements, including aircraft, radiosonde and ground-based GPS measurements (Gettelman et al., 2004; Zhan and Li, 2008; Qin et al., 2012). Their results have shown that retrievals of water vapor agree well with observational data and that AIRS products produce an average negative bias of 2 mm for precipitable water vapor. A recent study by Ni et al. (2013) showed that AIRS temperature profiles over the TP and the surrounding areas have a small bias at low levels and better agreement with radiosonde observations sounding profiles in the mid–upper levels of the atmosphere. The AIRS mixing ratio of water vapor is less than that of sounding data at low levels, and consistent with sounding data at higher levels.

A number of researchers have also used AIRS data to investigate synoptic systems. For example, the vertical thermodynamic structure and spatiotemporal evolution of the Madden–Julian oscillation (MJO) was analyzed by Tian et al. (2006), through the combined use of AIRS temperature and moisture data and TRMM (Tropical Rainfall Measuring Mission) precipitation data. The results showed that AIRS data can be used to capture the variation of the MJO as predicted by friction Kelvin–Rossby wave or CISK (Conditional Instability of the Second Kind) theory. Randel and Park (2006) explored the variability of Asian monsoon circulation and trace constituents linked to transient deep convection by using dynamical fields and AIRS data.

AIRS data have also been used extensively in numerical models. The use of AIRS profiles in ensemble forecast models can improve forecasts of convective weather. The assimilation of AIRS temperature and moisture profiles applied in the 3D-VAR (three-dimensional variational) data assimilation scheme of MM5 [Fifth-generation Pennsylvania State University–NCAR Mesoscale Model] significantly influences the location and intensity of simulated precipitation, and the spatial distribution of simulated precipitation is more representative of actual events (Singh et al., 2008, 2011; Jones and Stensrud, 2012). Overall, these results highlight the potential of using AIRS data for the TP and the Sichuan Basin. In particular, AIRS coverage can compensate for insufficient sounding data in these regions. To the best of our knowledge, the present study is the first to examine the SWV using AIRS data.

Because AIRS provides observations only twice daily, it is insufficient for analyzing the evolution of the SWV. Thus, a combination of recent AIRS observations and traditional observational data may provide greater insight into the characteristics of SWV processes. In the present study, a regional torrential rain process caused by the SWV on 10–14 July 2012 is analyzed using a combination of AIRS data, Final Operational Global Analysis (FNL) data, SWV intensive experiment data, and Meteorological Information Comprehensive Analysis and Process System (MICAPS) data. In addition, we explore the suitability of using AIRS data for studying the SWV and related severe synoptic systems over the TP and its surrounding areas.

2. Data and method

2.1. *AIRS, intensive sounding measurements, and ground measurements*

The data used in this paper include AIRS data, L-band intensive sounding data collected from SWV experiments, FNL data, and MICAPS data, for 10–14 July 2012. Developed by the China Meteorological Administration (CMA), MICAPS is a modern full-purpose forecaster workstation system used for processing and displaying meteorological data that can display meteorological information, geographical data, and historical meteorological data. MICAPS data represent a type of meteorological observation data. In this paper, we use grid-

Table 1. Information on the AIRS products used in this paper.

Characteristic	Name	Type	Level	Version
Brightness temperature	Brightness_temp	AIRABRAD	1B	5
Cloud water content	lwCDSup	AIRX2SUP	2	5
Outgoing long-wave radiance	olr	AIRX2SUP	2	5
Air temperature	TAirStd	AIRX2RET	2	5
Water vapor mixing ratio	H2OMMStd	AIRX2RET	2	5

ded data with a horizontal resolution of $2.5^\circ \times 2.5^\circ$. The data were recorded each day at 0000 and 1200 UTC. The FNL data were provided by the NCEP–NCAR. The encoding format version was GRIB1 (gridded binary formation), which is recommended by the WMO, and the data have not been assimilated. We chose a horizontal resolution of $1^\circ \times 1^\circ$ and a temporal resolution of 6 h. Data were recorded each day at 0000, 0600, 1200 and 1800 UTC.

The main task of AIRS is to detect the atmospheric temperature and generate moisture profiles from Earth's surface up to 40 km. The data of AIRS observations are saved in 240 files that correspond to 240 granules covering the globe twice daily (Goldberg et al., 2003). Each granule is composed of 135 scan lines, and each line has 90 observations, together forming the field of view (FOV). The L2 products, including the temperature and moisture profiles, are derived for each FOV with a horizontal spatial resolution of about 45 km in diameter at nadir. To reveal the development processes of the SWV, the AIRS products used in this study include the air temperature and the mixing ratio of water vapor, the cloud water content, outgoing longwave radiance, and brightness temperature. Validation by Divakarla et al. (2006) showed that that temperature and water vapor retrievals from version 4 of AIRS agree very well with radiosonde observations. The root-mean-square difference for clear-only cases over the "sea" and "all" categories was close to the expected goal accuracies; specifically, 1 K in 1-km layers for the temperature and better than 15% in 2-km layers for the water vapor in the troposphere were noted. In the present study, we mainly use the version 5 (V5) AIRS products. AIRS V5 retrievals make use of information originating from partly cloudy areas. Another critical element found in the AIRS V5 retrieval algorithm is the ability to generate case-by-case, level-by-level error estimates for the retrieved temperature profiles. These error estimates are used as part of the quality control procedure to assimilate AIRS temperature profiles (Susskind et al., 2011; Reale et al., 2012). Several studies have demonstrated the positive impact of quality-controlled AIRS V5 on a global data assimilation and forecasting system over different regions and for different weather systems (Reale et al., 2008; Zhou et al., 2010). Additional details of the AIRS V5 products can be found in Susskind et al. (2011). The AIRS products with quality flags equal to 0 and 1 are used in this study, as shown in Table 1.

L-band intensive sounding data, in which the observation and common sounding are performed four and two times a day, respectively, were collected from an intensive SWV experiment conducted during 21 June to 31 July 2012, by the Chengdu Institute of Plateau Meteorology in association with the CMA. Data from seven conventional radiosonde observation sounding sites (Ganzi, Hongyuan, Xichang, Yibin, Dazhou, Wenjiang, and Batang) are used in this study. The variables measured include atmospheric pressure, temperature, humidity, and wind direction and speed (Li et al., 2012). The precipitation data are from automatic weather stations.

2.2. *Computation of mixing ratio and potential temperature*

2.2.1. *Mixing ratio*

Because the mixing ratio and relative humidity are used to characterize humidity for AIRS and radiosonde observation, respectively, we calculated the mixing ratio of radiosonde observations for ease of comparison by using multiple parameters including temperature, pressure, and relative humidity (Dong and Tian, 1986). First, the saturation vapor pressure e_s is computed by using temperature in a standard pressure layer:

$$e_{sw} = 6.1078 \exp\left[\frac{17.26(T-273.16)}{T-35.86}\right]; \tag{1}$$

$$e_{si} = 6.1078 \exp\left[\frac{21.8746(T-273.16)}{T-7.66}\right]; \tag{2}$$

$$e_s = \begin{cases} e_{sw}, & (T \geqslant 258.16) \\ e_{si}, & (T \leqslant 233.16) \\ 0.022\{[80+2(T-273.16)]e_{sw} - [30+2(T-273.16)]e_{si}\}, & (233.16 < T < 258.16) \end{cases}; \tag{3}$$

where e_{sw} and e_{si} represent saturation vapor pressure (hPa) with respect to the liquid phase and the ice phase, respectively; p represents air pressure (hPa); and T is the temperature (K). Then, we can compute the vapor pressure e (hPa) as

$$e = e_s f\,, \tag{4}$$

where f represents relative humidity (100%). The mixing

ratio, r (g kg^{-1}), can be computed as

$$r = \frac{622e}{p-e}. \tag{5}$$

2.2.2. *Potential temperature*

Potential temperature is the temperature of an air mass if it were moved to standard pressure through dry adiabatic processes. According to this definition, the formula for calculating potential temperature is (Sheng et al., 2003)

$$\theta = T\left(\frac{p_{00}}{p}\right)^{0.286}, \tag{6}$$

where θ is potential temperature (K), T is the temperature (K), p_{00} is the standard pressure (hPa), and p is the pressure (hPa) of the original layer.

3. Synoptic discussion

3.1. *Characteristics of torrential rain*

The SWV over Southwest China is a mesoscale vortex with a horizontal scale of 200–600 km, and is one of the most important rain-producing systems in China during the summer months. As Zhang et al. (2015) showed, most SWVs are quasi-stationary, not moving out, but a small proportion can migrate eastwards. When an SWV migrates eastwards from Southwest China towards East China, it develops into a severe synoptic system that causes rainstorms along its path (Fu et al., 2011; Li and Deng, 2013). In this study, a rainstorm event during 10–14 July 2012, caused by an SWV, was selected for analysis. Both Sichuan Province and Chongqing municipality experienced intense rainfall associated with this event. The location of the precipitation area was at the intersection of Sichuan, Chongqing, and Guizhou. The amount of accumulated precipitation in this area reached the level of rainstorm at 281.1 mm, as observed over a 12-h period from 0400 UTC to 1600 UTC on 11 July at Wanyuan, where this SWV-driven rainstorm was centered. The variation in hourly precipitation during this event is shown in Fig. 1. To study the relationship between vorticity and precipitation, we analyzed the time series of precipitation and vorticity in Wanyuan. As shown in the figure, the vorticity was positive from 0400 UTC 9 July to 0400 UTC 13 July, with an increase from 1000 UTC 10 July until the maximum occurred at 0400 UTC 12 July. After 0400 UTC 13 July, the vorticity became negative and continued to decrease. The precipitation occurred mainly during the phase showing an increase in vorticity.

3.2. *3D structure of the SWV*

3.2.1. *Circulation pattern and temporal evolution*

The cyclonic circulation of an SWV appears mainly at 700 and 850 hPa, particularly at 700 hPa. According to the distribution of the vortex at 700 hPa from the MICAPS data (not shown), the SWV of concern in the present study emerged at 1200 UTC 10 July, moved eastwards during its temporal evolution, and reached its puissant phase at 0000 UTC 12 July. From 0000 UTC 12 July to 1200 UTC 12 July, it stagnated in the Chongqing area (30°N, 108°E), with the vortex intensity becoming slightly diminished at the center. At 0000 UTC 13 July, the SWV moved into Yunnan Province (27.5°N, 105°E), with a slight increase in vortex intensity at the center. At 1200 UTC 13 July, it moved into the junction of Hubei and Hunan provinces (30°N, 110°E), with the vortex intensity once again enhanced at the center, before moving eastwards and gradually dying out. The paths of this SWV's movement are shown in Fig. 2.

3.2.2. *Vertical evolution*

In order to study the vertical development of the SWV, we analyzed the vertical distribution of vorticity near 95°–115°E based on the FNL data. The meridional vertical vorticity

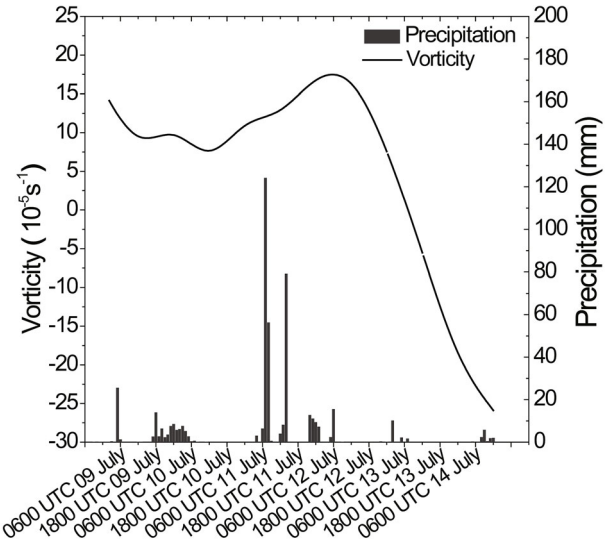

Fig. 1. Temporal series of precipitation and vorticity during 9–14 July 2012, in Dazhou.

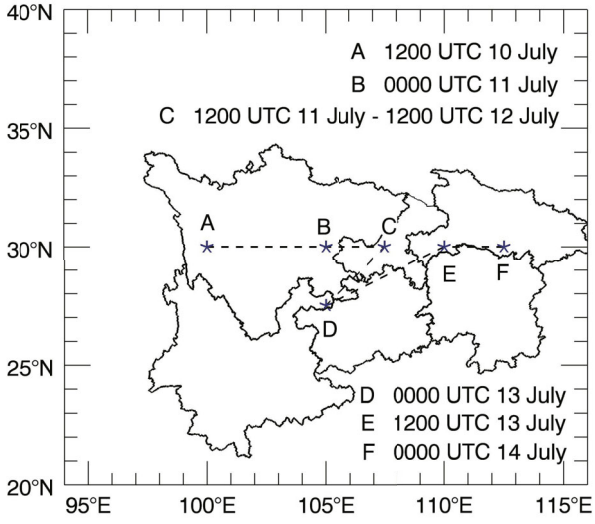

Fig. 2. Pathway of the SWV from 1200 UTC 10 July to 0000 UTC 14 July.

cross sections at 31°N (Fig. 3) illustrate the vertical structure of the SWV and its evolution.

In the nascent phase of the SWV (Fig. 3a), the maximum vertical vorticity was 8×10^{-15} s^{-1} and the center appeared at 700 hPa, located at 106°E. During the developing phase (Fig. 3b), the center of vorticity was raised to above 700 hPa, indicating the presence of incidental upward extensions in this period. However, the vorticity maximum in the vertical direction was nearly equal to that in the nascent phase, and the horizontal movement was not obvious. Furthermore, it is noteworthy that, in the west of the vortex center, an anticyclone appeared that was helpful for the SWV's development. In the puissant phase (Fig. 3c), the center of vorticity appeared at 700 hPa, with a maximum vorticity of 10×10^{-5} s^{-1}, located at 107°E. In the receding phase (Fig. 3d), the center of vorticity was divided into two parts. The first stagnated at 106°E, with a maximum of 6×10^{-5} s^{-1}, and the other moved to 110°E, with a maximum vorticity of 8×10^{-5} s^{-1}. In the case of this SWV, the vertical development of vorticity was not intense, and the vorticity showed an obvious decreasing trend when reaching the puissant phase.

3.2.3. *Moisture condition*

To analyze the transport of water vapor, we calculated the divergence of moisture flux from 1000 hPa to 700 hPa. The horizontal distributions of moisture flux divergence are shown in Fig. 4. The distribution before precipitation in the Wanyuan region, where the maximum precipitation center was located, showed a negative center value, implying intense vapor transport in this area. This continuous transport of water vapor provided favorable conditions for rainstorm formation.

4. Results and discussion

To improve the reliability of the diagnostic capabilities of AIRS data for SWVs, we first analyzed the applicability of AIRS data to the Sichuan region by comparing the AIRS temperature and humidity profiles with radiosonde observations for 1–31 July 2012. Data from Yibin and Xichang stations were selected to represent typical conditions in the Sichuan Basin and Western Sichuan Plateau. From the comparison of temperature and humidity profiles of two typical stations in these areas (figure not shown), we assumed that the temperature profile from AIRS has a high goodness-of-fit with radiosonde data in the Sichuan Basin and Western Sichuan Plateau and can be applied in studying synoptic systems in the Sichuan region.

4.1. *SWV characteristics from AIRS data*

4.1.1. *Vertical variation of potential temperature*

Potential temperature is an important temperature parameter of dry air. Because it is conserved through dry adiabatic

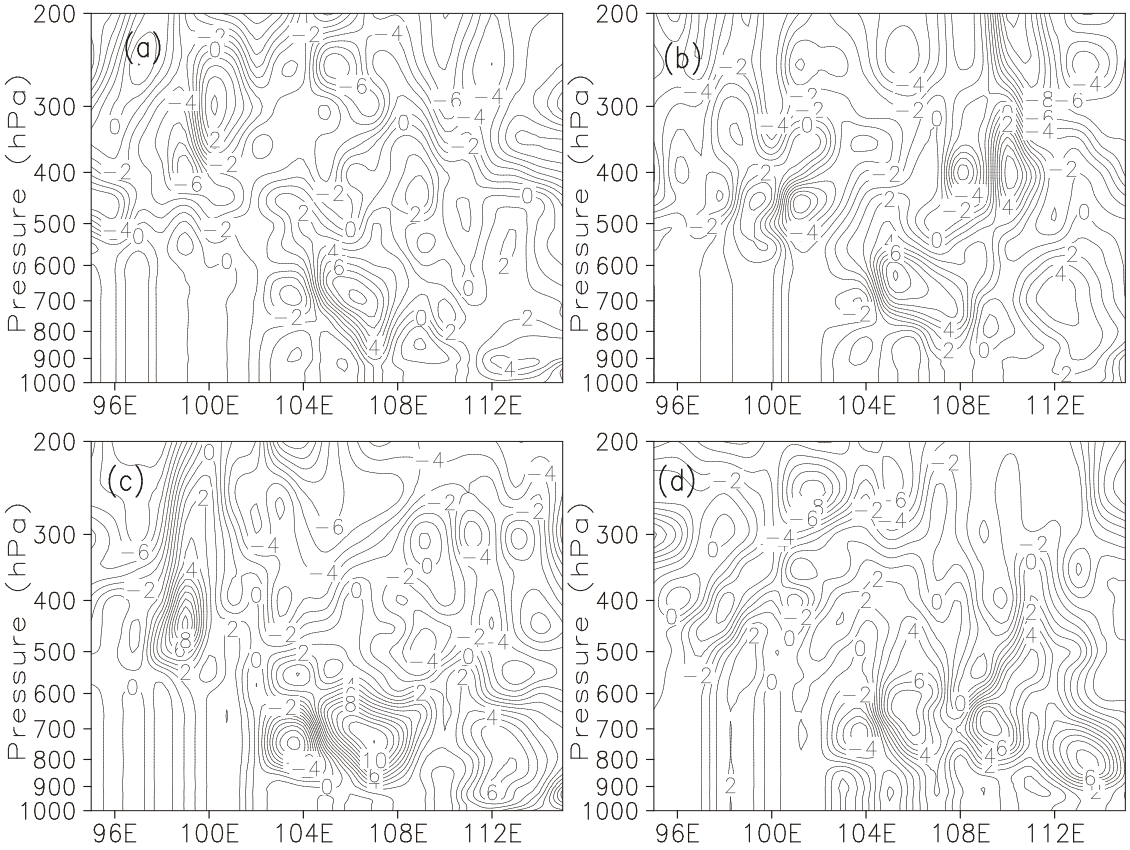

Fig. 3. Meridional vertical cross section of vorticity along 95°–115°E at 31°N (units: 10^{-5} s^{-1}): (a) 0000 UTC 11 July; (b) 0600 UTC 11 July; (c) 1800 UTC 11 July; (d) 0600 UTC 12 July.

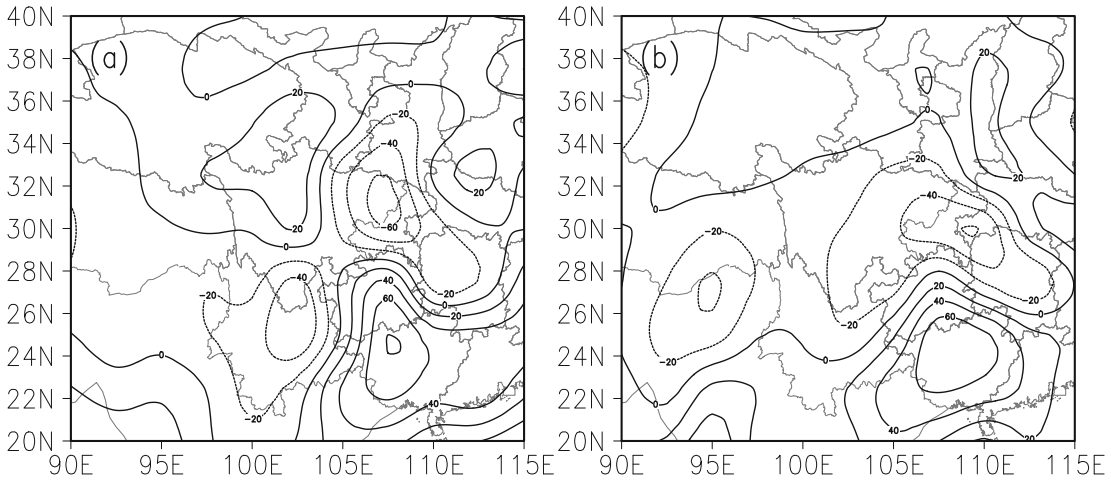

Fig. 4. Horizontal distribution of moisture flux divergence vertically integrated from 1000 hPa to 700 hPa (units: 10^{-6} g cm^{-2} s^{-2}): (a) 0000 UTC 10 July; (b) 0000 UTC 11 July.

processes, it can be used to compare the thermal differences of air mass under different air pressures. However, potential temperature is not conserved when there is a release of latent heat. We can evaluate atmospheric stability by using vertical variation rate profiles of potential temperature as (Sheng et al., 2003)

$$\frac{\partial\theta}{\partial z} = \frac{\theta}{T}(\gamma_{\rm v} - \Gamma) \approx \frac{\theta}{T}(\gamma_{\rm d} - \Gamma), \tag{7}$$

where θ is the potential temperature calculated from Eq. (6), Γ is the temperature lapse rate of a stratified atmosphere, γ_v is the temperature lapse rate of humid air, and $\gamma_{\rm d}$ is the temperature lapse rate of dry air. When $\partial\theta/\partial z > 0$ and $(\gamma_{\rm d} - \Gamma) > 0$, the atmosphere is stable; when $\partial\theta/\partial z < 0$ and $(\gamma_{\rm d} - \Gamma) < 0$, the atmospheric condition is unstable.

In the following analysis, the vertical variation rate profiles of potential temperature in Wanyuan before and after precipitation are presented; potential temperature was obtained using the Poisson formula in Eq. (6). The AIRS scanning time and footprint coordinates are included in Table 2, and the vertical variation profiles of potential temperature before and after precipitation are depicted in Fig. 5.

As shown in Fig. 5, potential temperature vertical variations for whole layers are negative, and the entire atmosphere is unstable, particularly below 10 000 gpm prior to precipitation. When rainfall occurred, the vertical variation in potential temperature for whole layers became positive. This phenomenon implies that the process of rainfall releases instability energy of the atmosphere; thus, the stability of atmospheric stratification increases after rainfall.

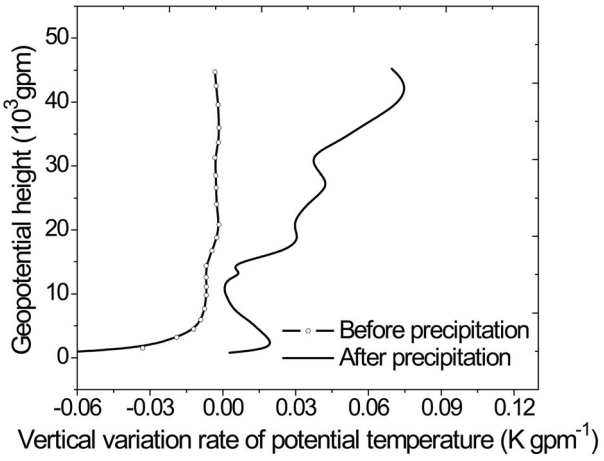

Fig. 5. Vertical variation in the potential temperature profile before and after precipitation in Wanyuan (units: K gpm^{-1}). The *x*-axis is the vertical variation of potential temperature (units: K gpm^{-1}) and the *y*-axis is geopotential height (units: gpm) (detailed information is shown in Table 2).

4.1.2. *Variation in cloud water content*

Cloud water content is a key parameter for describing the characteristics of clouds and moisture and is a primary indicator of the potential for artificial precipitation. Cloud moisture plays a key role in the occurrence of rainfall. Therefore, it can be used to aid the forecasting of rainstorms, and the variation of cloud water content can provide insight into the physical mechanism of precipitation. Many studies have revealed

Table 2. AIRS granule number and scanning time and the coordinates of AIRS footprint before precipitation and after precipitation.

	AIRS granule number (UTC)	AIRS scanning time (UTC)	AIRS footprint coordinates	Maximum precipitation coordinates	Distance (km)
Before precipitation	058 (10 July)	0548 UTC (10 July)	(31.94°N, 107.54°E)	(32.00°N, 107.81°E)	23
After precipitation	186 (11 July)	1836 UTC (11 July)	(31.96°N, 108.02°E)	(32.00°N, 107.81°E)	21

that the precipitation amount depends strongly on cloud water content and that these parameters are correlated (Ding et al., 2011; Li and Niu, 2012).

The variation in cloud water content before and after rainfall in Wanyuan was analyzed by using the cloud water content data from AIRS. The AIRS scanning time and footprint coordinates are shown in Table 2 and in Fig. 6. It is evident that cloud water content significantly increases after precipitation; its unit increased approximately two magnitudes once precipitation began. However, the vertical distribution of cloud water content showed little variation, with large values at low levels and smaller values at high levels.

To verify the reliability of AIRS cloud water content data, we analyzed the relationship between FNL precipitation and cloud water content data (figure not shown). The result shows that the period of maximum precipitation is inconsistent with the period of maximum cloud water content because the magnitude of precipitation is not dependent on cloud water content only; it is also related to cloud particle concentration, water vapor transport conditions, and other factors. At 0700 UTC 11 July, the FNL cloud water content showed a significant increase and reached a peak after heavy rainfall, which can be attributed to the increased evaporation of the underlying surface water after a rainfall event. Su et al. (2003) concluded that cloud water content increases after precipitation events and that the distribution of cloud water content can be depicted as unimodal in type by detecting the physical characteristics of precipitation clouds.

4.1.3. *Variation in OLR*

OLR is the energy radiating from Earth as infrared radiation at low energy to space. OLR is a critical component of Earth's energy budget and represents the total radiation emitted to space by the atmosphere (Susskind et al., 2011). The OLR is affected by clouds and dust in the atmosphere, which tend to reduce it to below clear-sky values.

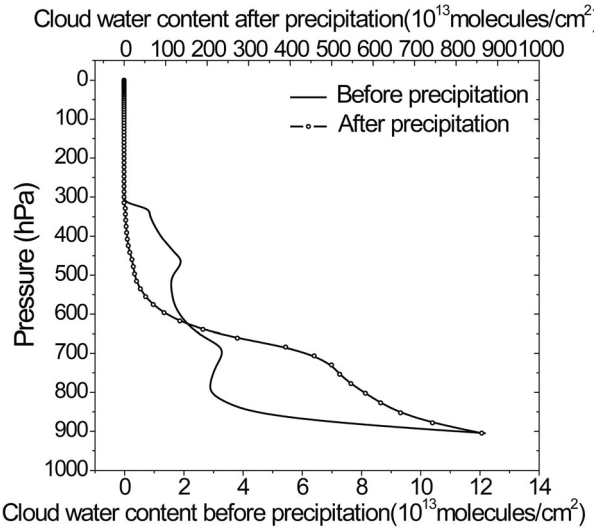

Fig. 6. Cloud water content profile before and after maximum precipitation, from AIRS (units: 10^{13} molecules cm^{-2}) (detailed information shown in Table 2).

The granule numbers of AIRS OLR data were 188 (9 July), 186 (11 July), and 063 (13 July). The AIRS OLR data in Fig. 7 indicate that the developing phase of the SWV was from 1848 UTC 9 July to 1836 UTC 11 July (Figs. 7a and b). During this phase, the value of OLR was obviously lower in Sichuan, Chongqing and Guizhou compared with other areas. With the eastward movement of the SWV and its shift to the puissant phase, the area with low OLR values moved eastwards, and the OLR value further reduced. Subsequently, the area of low OLR values moved gradually eastwards and finally left Sichuan and Chongqing. At 0618 UTC 13 July (Fig. 7c), the area with low OLR values moved into Hunan and Hubei provinces. From the movement of the low OLR area, we determined that the propagation path of the area with low OLR values is consistent with the path of the SWV.

4.1.4. *Change in the temperature of brightness blackbody*

Cloud top brightness temperature is the outward radiation of cloud tops obtained from infrared detection channels in meteorological satellites. In cloudless areas, it reflects the outward radiation of Earth's surface. Cloud top brightness temperature is the most primitive measurement for generating infrared images and various enhanced cloud pictures and is equivalent to the temperature of brightness blackbody (TBB). In cloudy regions, TBB is the blackbody radiation temperature at cloud tops; low TBB values correspond to higher cloud tops and more vigorous convection.

Thus, TBB can reveal the existence of clouds and some significant characteristics of the phase of evolution of clouds. In addition, TBB values display the relationship with surface precipitation to some extent (Cao et al., 2013). Fei et al. (2008) revised the minimum scale criteria for the β-MCS (mesoscale convective system) census according to the scaled classification criteria proposed by Orlanski (1975). They revised the criteria so that the TBB values were less than or equal to 241 K and the diameters of continuous cold cloud areas were greater than 20 km. In addition, they mentioned that TBB values less than or equal to 221 K indicate deep convection. The granule numbers for the AIRS TBB data are the same as those for the OLR data.

The time series of TBB depicted in Fig. 8 shows that, at 1848 UTC 9 July, there was no obvious low TBB area. At 1836 UTC 11 July (Fig. 8b), an obvious low TBB area appeared at the junction of Sichuan, Guizhou and southern Chongqing, with a TBB value of approximately 230 K. Then, the low TBB area disappeared at 0618 UTC 13 July. Through a diagnostic analysis of a rainstorm event, Wang and Cheng (2013) determined that lower TBB values within a certain range are indicative of more intense precipitation. The time that the obviously low TBB area appeared coincided with the time at which the SWV reached its puissant phase, which also coincided with periods of heavy precipitation. This phenomenon shows that TBB data can reflect the development of MCS and has a strong relationship with precipitation intensity.

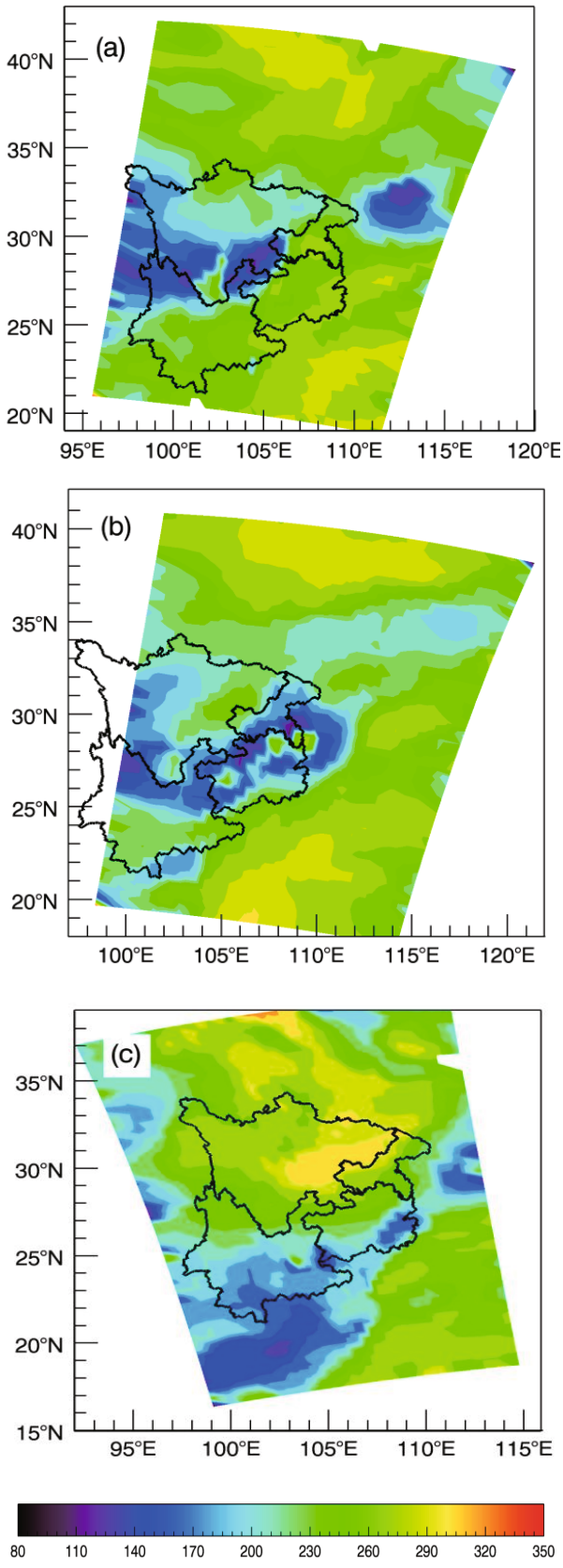

Fig. 7. Outgoing longwave radiation data in AIRS (units: W m^{-2}): (a) 1848 UTC 9 July; (b) 1836 UTC 11 July; (c) 0618 UTC 13 July.

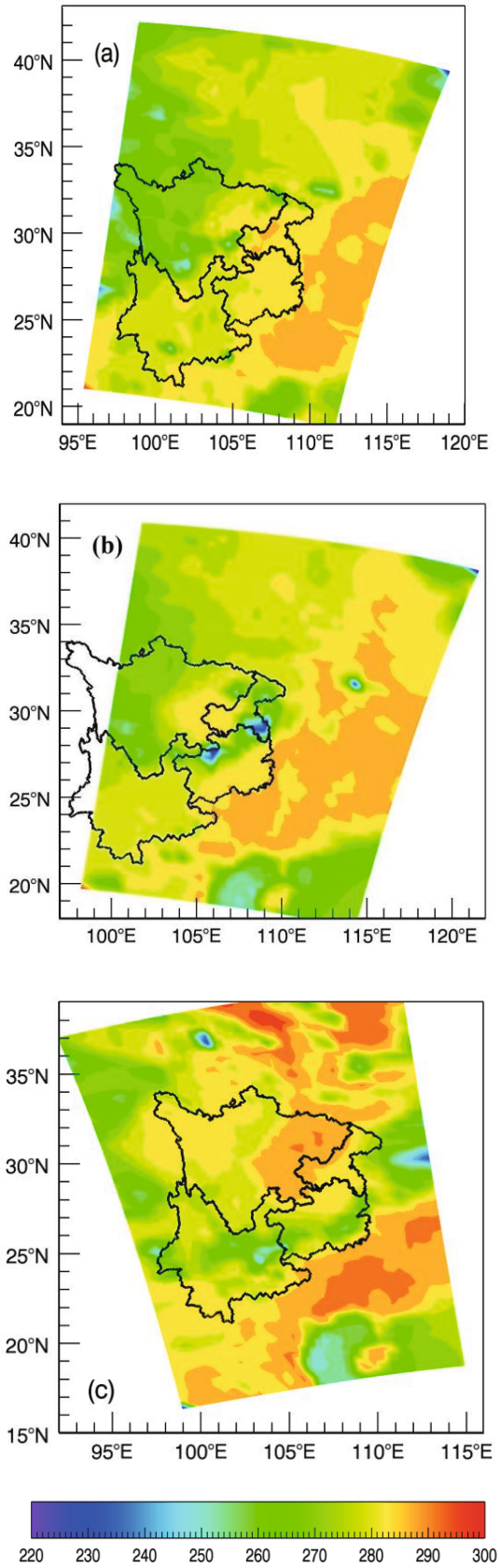

Fig. 8. Cloud top brightness temperature from AIRS (units: K): (a) 1848 UTC 9 July; (b) 1836 UTC 11 July; (c) 0618 UTC 13 July.

4.1.5. *Changes in temperature and humidity profiles in different phases of the SWV*

According to vortex data at 700 hPa collected using MICAPS, this SWV process can be divided into seven phases: nascent, developing, puissant, receding, redevelopment, new puissant, and perishing. The corresponding times for each phase are shown in Table 3. According to the movement of the SWV (Fig. 2), the maximum vortex center was located at (30°N, 107.5°E) from 1200 UTC 11 July to 1200 UTC 12 July. To examine the changes in temperature and moisture caused by the SWV's movement, we analyzed the characteristics of temperature variation and mixing ratio profiles from the developing phase to the receding phase. The AIRS data used for this analysis are shown in Table 4.

We screened the coordinates of the maximum vorticity based on AIRS temperature and humidity profiles. As indicated by the distribution of temperature (Fig. 9a) and mixing ratio (Fig. 9b) from the developing phase to the receding phase, the change in temperature in the lower layers was small during the SWV's developing phase, and an isothermal layer existed with the temperature maintained at 285 K between 900 hPa and 600 hPa. In addition, the vertical temperature lapse rate was very small. When the evolution of the SWV approached the puissant phase, the temperature of the lower layers was greater than that during the developing phase, and the isothermal layer disappeared. When the SWV approached the receding phase, the temperature of the lower layers was smaller than that during the puissant phase, and the temperature below 500 hPa was slightly greater than that during the developing phase. As depicted in Fig. 9b, the moisture distribution of the whole layer showed a "low layers wet while high layers dry" pattern from the developing phase to the receding phase. During the puissant phase, the vertical distribution of the mixing ratio peaked at 900 hPa in the center of the SWV, and the layers beneath 900 hPa displayed a significant moisture inversion. When the SWV approached the receding phase, the water vapor content was obviously reduced compared with that in the developing and puissant phases. Moreover, the distribution of the mixing ratio fluctuated, and a moisture inversion occurred between 700 hPa and 500 hPa.

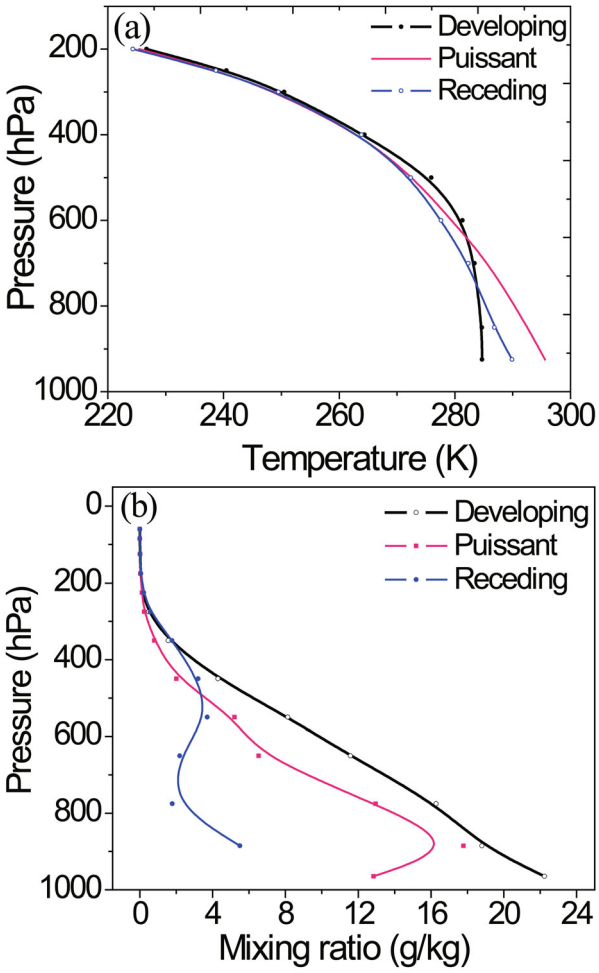

Fig. 9. The (a) temperature and the (b) mixing ratio profile from AIRS in the center of the SWV during the developing phase to receding phase (detailed information shown in Table 4).

To further investigate the reasons for the changes in moisture profiles and to analyze the transport of water vapor, we calculated the divergence of water vapor vertical flux from the surface to 300 hPa. To reduce the influence of moisture con-

Table 3. Corresponding time of each phase in the evolution of the SWV.

Name of phase	Time (UTC)	Name of phase	Time (UTC)
Nascent	0000 UTC 11 July	Redevelopment	0000 UTC 13 July
Developing	1200 UTC 11 July	Anew puissant	1200 UTC 13 July
Puissant	0000 UTC 12 July	Perishing	0000 UTC 14 July
Receding	1200 UTC 12 July		

Table 4. Scanning time and granule number of AIRS data used in three phases of the SWV, and the coordinates of the SWV and the AIRS footprint.

Name of phase	AIRS granule number (UTC)	AIRS scanning time (UTC)	Vortex coordinates	AIRS footprint coordinates
Developing	065 (11 July)	0630 UTC 11 July	(30°N, 105.0°E)	(29.94°N,104.88°E)
Puissant	186 (11 July)	1836 UTC 11 July	(30°N, 107.5°E)	(30.03°N, 107.54°E)
Receding	056 (12 July)	0536 UTC 12 July	(30 °N, 107.5°E)	(29.03°N, 108.02°E)

tent owing to the SWV's movement, we analyzed the vapor transport condition from the developing phase to the receding phase of the SWV. During this period, the SWV was stable at the junction of Sichuan and Chongqing. Torrential rain occurrence is often closely related to water vapor; a continuous supply of water vapor is a necessary condition for the formation, development, and occurrence of rainstorms. The vertical flux of vapor divergence characterizes the vertical transport of vapor flux divergence. Compared with vapor flux divergence, the vertical flux of vapor divergence can better describe the powerful rise, convergence and divergence movement associated with torrential rainfall and its water vapor transport conditions (Li and Deng, 2013). The distribution of the vertical flux of vapor divergence in this SWV process is shown in Fig. 10.

During the nascent and developing phases (Figs. 10a and b), the SWV was located in an area characterized by positive vertical moisture flux divergence, which is evidence of the vertical advection of moisture divergence. When the evolution of the SWV approached the puissant phase (Fig. 10c), the source of the SWV was the convergence center of the vertical flux of vapor divergence, which implies the presence of intense water vapor convergence compared with the intense vertical transport. Thus, as shown in Fig. 9a, the mixing ratio profiles during the puissant phase of the SWV indicate that the moisture inversion occurred below 900 hPa. Furthermore, the mixing ratio was underestimated with respect to observations during the developing phase. When the evolution of the SWV approached the receding phase (Fig. 10d), the value of the vertical flux of vapor divergence had reduced but was still positive. In addition, a rainfall process occurred during this phase, which caused the value of the mixing ratio to be less than that during the puissant phase.

5. Summary and conclusions

In this study, a comprehensive analysis of an SWV-related heavy rainfall event over South China in 2012 is performed using a combination of AIRS data, intensive sounding data, FNL reanalysis data, and MICAPS data. The results can be summarized as follows:

(1) The entire atmosphere was unstable before precipitation occurred. After rainfall, the potential temperature at different altitudes became positive, implying a release of instability energy in the atmosphere. In addition, the cloud water content in the atmosphere, as observed by AIRS, increased significantly after precipitation.

(2) Areas with low OLR were well correlated with the locations of the SWV, and the path of low-OLR areas was consistent with the path of the SWV.

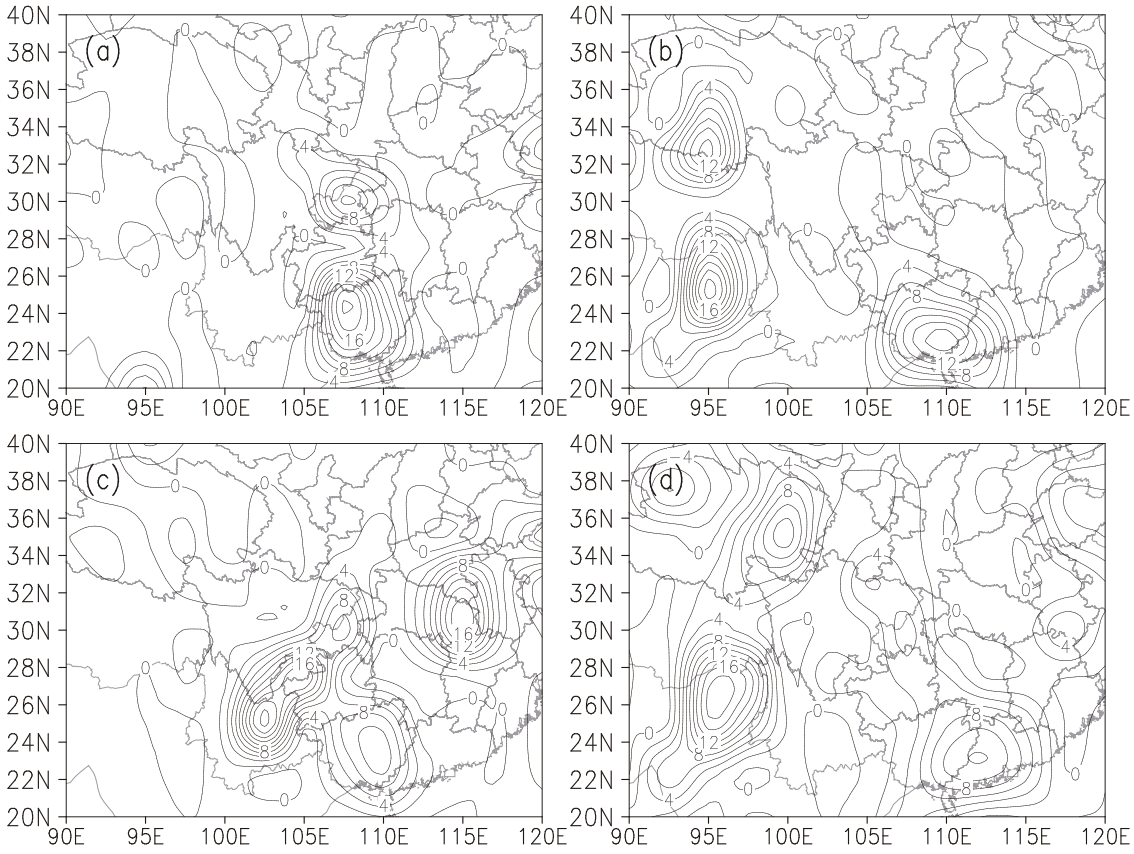

Fig. 10. Horizontal distribution of the vertical flux of vapor divergence vertically integrated from 1000 hPa to 300 hPa (units: 10^{-6} g Pa cm^{-2} s^{-2}): (a) 0000 UTC 11 July; (b) 1200 UTC 11 July; (c) 0000 UTC 12 July; (d) 1200 UTC 12 July.

(3) AIRS TBB data displayed low values until the SWV reached its puissant phase. This phenomenon indicates that AIRS TBB may reflect the development of mesoscale convective systems and is related to precipitation intensity.

(4) The isothermal layer observed between low and middle layers during the development phase disappeared when the event reached its peak intensity. During the puissant phase of the SWV, the vertical distribution of moisture displayed large variation, and moisture inversion occurred at low levels. The moisture content during the receding phase was obviously reduced compared with that during the developing and puissant phases. This change in moisture profile can be attributed to the vertical flux of vapor divergence.

This study helps to elucidate the vertical structure of an SWV event and indicates that AIRS temperature and moisture profiles can effectively help to explain its evolution. Further application of AIRS/AMSU sounding products in the analysis of SWV weather processes over the TP and the surrounding areas will be valuable owing to the limited availability of in situ observations in this region. However, these results are based only on a single torrential rainfall process caused by the SWV. Thus, further studies on other high-impact synoptic systems over the TP and the surrounding areas are required. Since successful application of AIRS data to SWV systems can be made, we can try to use it on other mesoscale synoptic systems over the TP. Based on the high resolution and reliability of AIRS data, we can also try to apply it in the WRF model for improving the forecasting ability of severe weather over the TP and its surrounding areas. Moreover, a comparison of SWV events with extreme precipitation produced by other types of convectively driven phenomena, such as African Easterly Waves and Mesoscale Convective Clusters, should be the subject of future investigations.

Acknowledgements. The authors would like to express their sincere thanks to the Plateau Meteorological Data Centre associated with the Chengdu Institute of Plateau Meteorology, CMA, which supplied the intensive sounding data for the SWV observation experiment. This work was supported by the Special Fund for Meteorological Research in the Public Interest (Grant No. GYHY201206042), and the National Natural Science Foundation of China (Grant No. 41675057, 91337215).

REFERENCES

Chang, C. P., L. Yi, and G. T. J. Chen, 2000: A numerical simulation of vortex development during the 1992 east Asian summer monsoon onset using the navy's regional model. *Mon. Wea. Rev.*, **128**(6), 1604–1631.

Chen, L. F., and K. Gao, 2007: The structure of Meiyu Front and the relationship between the front and the vortex disturbance along it. *Chinese J. Atmos. Sci.*, **31**(5), 863–875. (in Chinese)

Cao, Y., C. J. Yue, and S. W. Shou, 2013: Statistical synthesis on relationship between the number of convective core and the character of TBB within the tropical cyclone circulation and its intensity. *Journal of Tropical Meteorology*, **29**(3), 381–392. (in Chinese)

Ding, W. Y., Q. L. Wan, Y. Y. Huang, Z. T. Chen, and C. Z. Zhang, 2011: MODIS brightness temperature data assimilation under cloudy conditions II: Impacts on rainstorm forecasting. *Journal of Tropical Meteorology*, **17**(3), 221–230, doi: 10.3969/j.issn.1006-8775.2011.03.004.

Divakarla, M. G., C. D. Barnet, M. D. Goldberg, L. M. Mcmillin, E. Maddy, W. Wolf, L. H. Zhou, and X. P. Liu, 2006: Validation of Atmospheric Infrared Sounder temperature and water vapor retrievals with matched radiosonde measurements and forecasts. *J. Geophys. Res.*, **111**, D09S15, doi: 10.1029/2005JD006116.

Dong, X. M., and S. P. Tian, 1986: *Introduction of Diagnostic Analysis Method of Synoptic*. Meteorology Press, 164 pp. (in Chinese)

Fei, Z. P., Y. G. Zheng, Y. Zhang, and H. Q. Wang, 2008: MCS census and modification of MCS definition based on geostationary satellite infrared imagery. *Journal of Applied Meteorological Science*, **19**(1), 82–90. (in Chinese)

Fu, S. M., J. H. Sun, S. X. Zhao, and W. L. Li, 2011: The energy budget of a southwest vortex with heavy rainfall over south China. *Adv. Atmos. Sci.*, **28**(3), 709–724, doi: 10.1007/s00376-010-0026-z.

Fu, S. M., W. L. Li, J. H. Sun, J. P. Zhang, and Y. H. Zhang, 2015: Universal evolution mechanisms and energy conversion characteristics of long-lived mesoscale vortices over the Sichuan Basin. *Atmospheric Science Letters*, **16**(2), 127–134.

Gao, S. T., and F. Ping, 2005: An experiment study of lee vortex with large topography forcing. *Chinese Science Bulletin*, **50**, 248–255.

Gettelman, A., D. E. Kinnison, T. J. Dunkerton, and G. P. Brasseur, 2004: Impact of monsoon circulations on the upper troposphere and lower stratosphere. *J. Geophys. Res.*, **109**(D22), doi: 10.1029/2004JD004878.

Goldberg, M. D., Y. Qu, L. M. McMillin, W. Wolf, L. H. Zhou, and M. Divakarla, 2003: AIRS near-real-time products and algorithms in support of operational numerical weather prediction. *IEEE Trans. Geosci. Remote Sens.*, **41**(2), 379–389.

He, G. B., 2012: Review of the southwest vortex research. *Meteorological Monthly*, **38**(2), 155–163. (in Chinese)

Jones, T. A., and D. J. Stensrud, 2012: Assimilating AIRS temperature and mixing ratio profiles using an ensemble Kalman filter approach for convective-scale forecasts. *Wea. Forecasting*, **27**(3), 541–564.

Kuo, Y. H., L. S. Cheng, and R. A. Anthes, 1986: Mesoscale analyses of the Sichuan flood catastrophe, 11–15 July 1981. *Mon. Wea. Rev.*, **114**(11), 1984–2003.

Kuo, Y. H., L. S. Cheng, and J. W. Bao, 1988: Numerical simulation of the 1981 Sichuan flood. Part I: Evolution of a mesoscale southwest vortex. *Mon. Wea. Rev.*, **116**(12), 2841–2504.

Li, G. P., 2007: *Dynamic Meteorology of the Tibetan Plateau*. 2nd ed., China Meteorological Press, 271 pp. (in Chinese)

Li, G. P., and J. Deng, 2013: Atmospheric water monitoring by using ground-based GPS during heavy rains produced by TPV and SWV. *Advances in Meteorology*, **2013**, Article ID 793957, doi: 10.1155/2013/793957.

Li, J., J. Du, D.-L. Zhang, C. G. Cui, and Y. S. Liao, 2014: Ensemble-based analysis and sensitivity of mesoscale forecasts of a vortex over southwest China. *Quart. J. Roy. Meteor. Soc.*, **140**, 766–782.

Li, Y. Q., X. B. Zhao, L. H. Zhang, and C. C. Zhou, 2012: The intensive observation scientific experiment of southwest China

vortex in the summer of 2012. *Plateau and Mountain Meteorology Research*, **32**(4), 1–8. (in Chinese)

Li, Y. W., and S. J. Niu, 2012: The formation and precipitation mechanism of two ordered patterns of embedded convection in stratiform cloud. *Science China Earth Sciences*, **55**, 113–125, doi: 10.1007/s11430-011-4278-y.

Ni, C. C., G. P. Li, and X. Z. Xiong, 2013: Validation of the applicability of AIRS data in Sichuan-Tibet region of China. *Journal of Mountain Science*, **31**(6), 656–663. (in Chinese)

Orlanski, I., 1975: A rational subdivision of scales for atmospheric processes. *Bull. Amer. Meteor. Soc.*, **56**, 527–530.

Qin, J., K. Yang, T. Koike, H. Lu, Y. M. Ma, and X. D. Xu, 2012: Evaluation of AIRS precipitable water vapor against ground-based GPS measurements over the Tibetan Plateau and its surroundings. *J. Meteor. Soc. Japan*, **90C**, 87–98.

Randel, W. J., and M. Park, 2006: Deep convective influence on the Asian summer monsoon anticyclone and associated tracer variability observed with Atmospheric Infrared Sounder (AIRS). *J. Geophys. Res.*, **111**, D12314, doi: 10.1029/2005JD006490.

Reale, O., J. Susskind, R. Rosenberg, E. Brin, E. Liu, L. P. Riishojgaard, J. Terry, and J. C. Jusem, 2008: Improving forecast skill by assimilation of quality-controlled AIRS temperature retrievals under partially cloudy conditions. *Geophys. Res. Lett.*, **35**, L08809, doi: 10.1029/2007GL033002.

Reale, O., K. M. Lau, J. Susskind, and R. Rosenberg, 2012: AIRS impact on analysis and forecast of an extreme rainfall event (Indus River Valley, Pakistan, 2010) with a global data assimilation and forecast system. *Geophys. Res.*, **117**, D08103, doi: 10.1029/2011JD017093.

Sheng, P. X., J. T. Mao, J. G. Li, A. C. Zhang, J. G. Sang, and N. X. Pan, 2003: *The Atmospheric Physics*. Peking University Press, 522 pp. (in Chinese)

Singh, R., P. K. Pal, C. M. Kishtawal, and P. C. Joshi, 2008: Impact of Atmospheric Infrared Sounder data on the numerical simulation of a historical Mumbai rain event. *Wea. Forecasting*, **23**(5), 891–913.

Singh, R., C. M. Kishtawal, and P. K. Pal, 2011: Use of Atmospheric Infrared Sounder clear-sky and cloud-cleared radiances in the weather research and forecasting 3DVAR assimilation system for mesoscale weather predictions over the Indian region. *J. Geophys. Res.*, **116**, D22116, doi: 10.1029/2011JD016379.

Su, Z. J., W. G. Liu, G. H. Wang, C. H. Xu, and L. J. Wang, 2003: Microphysical characteristics of a precipitation process in Qinghai province. *Journal of Applied Meteorological Science*, **14**(S1), 27–35. (in Chinese)

Susskind, J., J. M. Blaisdell, L. Iredell, and F. Keita, 2011: Improved temperature sounding and quality control methodology using AIRS/AMSU data: The AIRS Science Team version 5 retrieval algorithm. *IEEE Trans. Geosci. Remote Sens.*, **49**, 883–907, doi: 10.1109/TGRS.2010.2070508.

Tao, S. Y., and Y. H. Ding, 1981: Observational evidence of the influence of the Qinghai-Xizang (Tibet) Plateau on the occurrence of heavy rain and severe convective storms in China. *Bull. Amer. Meteor. Soc.*, **62**(1), 23–30.

Tian, B. J., D. E. Waliser, E. J. Fetzer, B. H. Lambrigtsen, Y. L. Yung, and B. Wang, 2006: Vertical moist thermodynamic structure and spatial-temporal evolution of the MJO in AIRS observations. *J. Atmos. Sci.*, **63**(10), 2462–2485.

Wang, B., and I. Orlanski, 1987: Study of a heavy rain vortex formed over the eastern flank of the Tibetan Plateau. *Mon. Wea. Rev.*, **115**(7), 1370–1393.

Wang, Q. W., and Z. M. Tan, 2014: Multi-scale topographic control of southwest vortex formation in Tibetan Plateau region in an idealized simulation. *J. Geophys. Res.*, **119**(20), 11 543–11 561, doi: 10.1002/2014JD021898.

Wang, W., and P. Cheng, 2013: Numerical simulation and diagnostic analysis of heavy rainstorm on 27 July 2012 in north Shaanxi. *Transactions of Atmospheric Sciences*, **36**(2), 174–183. (in Chinese)

Wang, W., Y. H. Kuo, and T. T. Warner, 1993: A diabatically driven mesoscale vortex in the lee of the Tibetan Plateau. *Mon. Wea. Rev.*, **121**(9), 2542–2561.

Zhan, R. F., and J. P. Li, 2008: Validation and Characteristics of upper tropospheric water vapor over the Tibetan Plateau from AIRS satellite retrieval. *Chinese J. Atmos. Sci.*, **32**(2), 242–260. (in Chinese)

Zhang, J. P., S. M. Fu, J. H. Sun, X. Y. Shen, and Y. C. Zhang, 2015: A statistical and compositional study on the two types of mesoscale vortices over the Yangtze River Basin. *Climatic and Environmental Research*, **20**(3), 319–336. (in Chinese)

Zhong R., L. H. Zhong, L. J. Hua, and S. D. Feng, 2014: A climatology of the southwest vortex during 1979–2008. *Atmospheric and Oceanic Science Letters*, **7**(6), 577–583.

Zhou, Y. P., K. M. Lau, O. Reale, and R. Rosenberg, 2010: AIRS impact on precipitation analysis and forecast of tropical cyclones in a global data assimilation and forecast system. *Geophys. Res. Lett.*, **37**, L02806, doi: 10.1029/2009GL041494.